ORIGINAL ARTICLE

Analytical and experimental study on the surface generation mechanism in two-dimensional ultrasonic-assisted grinding of silicon carbide

Hongbo Li[1] · Tao Chen[1] · Zhenyan Duan[1] · Yiwen Zhang[1] · Haotian Li[1]

Abstract

Two-dimensional ultrasonic-assisted grinding (2D-UAG) is generally considered as an effective machining method for hard and brittle materials. However, due to the complicated grinding kinematics and material removal behaviors, the surface generation mechanism in 2D-UAG still has not been elaborately addressed. In this study, a numerical model considering the dynamic cutting behaviors of multiple abrasive grits and the material removal mechanism of silicon carbide (SiC) is proposed to reveal the kinematic characteristics during grinding and to predict the surface roughness. In the model development, a single abrasive grain is simplified as a cutting point and the cutting depth of individual grit is obtained based on the positional relationships among trajectory points. Theoretical analysis indicates that the cutting depth of abrasive grits in 2D-UAG approximately follows the normal distribution, which is similar with that in conventional grinding (CG). The introduction of two-dimensional ultrasonic vibration significantly alters the distribution ranges and characteristics of cutting speed and cutting angles of active grains relative to the workpiece. The experimental results demonstrate that the prediction error of this model is limited within 10.06%. Furthermore, in the machining conditions discussed in this study where the electroplated diamond grinding wheel with a grit size of 240# is used, the workpiece material is mainly removed by brittle fracture. Expanding the distribution range of the cutting angle in the YOZ plane can effectively suppress the adverse influences of nonuniform grain protrusion height and reduce the groove depth on machined surfaces, which are conducive to improve the ground surface quality.

Keywords Two-dimensional ultrasonic-assisted grinding · Silicon carbide · Kinematic characteristics · Surface generation mechanism

1 Introduction

Silicon carbide (SiC) has been applied in various industrial fields attributed to excellent physical and chemical properties [1, 2]. However, due to machining-induced defects and severe tool wear caused by its high hardness and low fracture toughness, conventional machining methods for metal materials are not suitable for SiC [3]. Ultrasonic-assisted grinding (UAG) is generally considered as a superior machining solution for hard and brittle materials [4]. Compared with conventional grinding (CG), this hybrid processing method can effectively reduce

grinding forces and improve machined surface quality [5]. To preliminarily reveal the material removal mechanism of brittle materials during grinding, scholars have performed a series of simulations and scratching tests. Li et al. [6] conducted a varied-depth scratching test on SiC workpiece using a Berkovich indenter and observed the surface micro-topography by a scanning electron microscope (SEM). The deformation behaviors of SiC demonstrated that as the scratching depth increased, the material removal mode shifted from plastic deformation to brittle fracture. Based on a self-designed machining system, Cao et al. [7] carried out ultrasonic-assisted scratching (UAS) tests of SiC ceramic. The experimental results indicated that the application of ultrasonic vibration can effectively improve the material removal rate and the critical depth of cut in UAS increased by 56.25% compared with that in conventional scratching. Liu et al. [8] performed single-grain scratching simulations using smoothed particle hydrodynamics (SPH) methodology. The simulation results indicated that increasing wheel speed was

✉ Tao Chen
chent29@whut.edu.cn

[1] School of Mechanical and Electronic Engineering, Wuhan University of Technology, Wuhan 430070, People's Republic of China

beneficial to transform the deep longitudinal crack to shallow lateral crack by providing a higher strain rate, which was verified experimentally. Dai et al. [9] performed single-diamond scratching tests on SiC at different wheel speeds. By observing the surface and subsurface topographies of the scratching grooves, they found that with the increase of scratching depth, the machining process went through four stages including ductile stage, primarily ductile stage, primarily brittle stage, and brittle stage. Furthermore, dislocations and amorphization of SiC grains represented the plastic deformation mechanism of workpiece, while the stress concentration resulted from dislocation pile-ups was responsible for the brittle crack initiation. According to the specific grinding energy in elliptical ultrasonic-assisted grinding (EUAG) of brittle materials, Chen et al. [10] proposed a theoretical model to predict the critical undeformed chip thickness, which was verified by experiments. The results showed that the critical value increased with the increase of spindle speed, axial ultrasonic amplitude, and ultrasonic frequency.

To further reveal the surface generation mechanism during grinding, recent researches have considered the coupling effects between adjacent abrasive grains. Based on the kinematic characteristics of neighboring abrasive grits in UAG, a grit-workpiece contact rate model was proposed and verified experimentally by Yang et al. [11]. This theoretical model can be employed to determine the intermittent processing matching conditions and to reveal the influences of machining parameters on the contact rate between abrasive grains and workpiece. Cao et al. [12] obtained the undeformed chip thickness of individual grit in tangential ultrasonic vibration-assisted profile grinding (UVAPG) according to the motion trajectories of adjacent grits. A prediction model of grinding wheel wear volume was further developed and validated by experiments. To reveal the matching relationship between cutting parameters and ultrasonic parameters, Zhou et al. [13] proposed a novel concept named matching phase difference (MPD) and established a machined surface topography prediction model. The results indicated that when the MPD was π, the interference effects of multiple rotation cycles became strongest and the minimum surface roughness can be gained.

In real grinding situations, the abrasive grains are distributed on the grinding wheel surface unevenly with different sizes and shapes and the machined surface is formed by a large number of abrasive grits. Therefore, it is difficult to accurately describe the dynamic material removal behavior and the complex surface generation mechanism during the grinding process by considering only a few neighboring grits. To address this issue, the coupling effects among multiple abrasive grains were taken into account in recent studies. Based on the assumption that the abrasive grits are uniformly spaced on the grinding tool surface and the grain protrusion height follows a normal distribution, Setti et al. [14] proposed a theoretical model to obtain the undeformed chip thickness in micro grinding. In the model development, the motion trajectories of a group of abrasive particles with the identical axial position were considered. This model revealed the differences between micro grinding and conventional grinding from a kinematic point of view. By quantifying the interference and overlap phenomenon of grain trajectories, Zhang et al. [15] proposed a kinematic model to understand the surface generation mechanism in ultrasonic vibration-assisted face grinding. Based on this model, the machined surface morphology can be manipulated by adjusting the machining parameters. Wu et al. [16] first measured the surface topography of a multi-hump grinding tool using a laser displacement sensor system. Combined with the material removal mechanism of advanced ceramics, a surface roughness prediction model was further proposed, which was validated experimentally with an average prediction error of 15%. Sun et al. [17] fabricated a grinding tool with helical chip pockets using a wire electrical discharge machining system and reconstructed the three-dimensional surface morphology of the tool considering grit size and distribution. After that, a prediction model of machined surface topography was established according to grinding kinematics. Experimental validation showed that the average prediction error of surface roughness was 5%. Through dividing the grinding wheel used in gear profile grinding into slices vertical to its axis, Zhou et al. [18] simulated its three-dimensional surface morphology. Considering the geometric contact characteristics, a comprehensive model was developed to predict the machined surface topography. This model can reveal the influences of machining parameters on the texture pattern and surface roughness distribution of the tooth surface. Zhou et al. [19] proposed a theoretical model for UAG with the consideration of Poisson effect and grinding wheel topography to predict the machined surface morphology. The results showed that the introduction of axial ultrasonic vibration was beneficial to gain uniform undeformed chip thickness and to reduce the surface roughness value. Using a similar methodology, Wang et al. [20] established a surface morphology prediction model in EUAG of monocrystal silicon. They found that applying ultrasonic vibration perpendicular to the machined surface can improve the material removal rate, whereas the surface roughness value increased with increasing vertical ultrasonic amplitude.

Although the above-mentioned studies have realized the prediction of surface roughness, less specific information on the kinematic characteristics of abrasive grains during the grinding process is available. In two-dimensional ultrasonic-assisted grinding (2D-UAG), the motion trajectory of abrasive grains becomes more complex and the coupling effects among grits are more pronounced. Revealing the kinematic features and material removal behaviors during grinding considering multiple abrasive grits is of great importance to understand the machining mechanism of this hybrid processing method and to optimize the machining parameters.

In this study, based on the size characteristics of abrasive grains and the material removal mechanism, a numerical model is proposed to reveal the cutting behaviors and the

surface generation mechanism in 2D-UAG of SiC. In the model development, it is assumed that the abrasive grains are uniformly distributed on the grinding wheel surface and a group of grits with the same axial position is taken into consideration. A single grit is simplified as a cutting point and the cutting depth of individual grit is calculated according to the positional relationship among trajectory points. Based on the theoretical model, the statistical characteristics of the cutting depth, the cutting speed, and the cutting angles of active grits can be gained to reveal the kinematic features in 2D-UAG. Furthermore, the surface roughness along the feed direction is calculated based on the machined surface profile. Finally, experiments are conducted to validate the proposed model and obtain the microscopic morphology of machined surfaces.

2 Theoretical analyses

2.1 Kinematic model

The schematic diagram of the 2D-UAG process is illustrated in Fig. 1. During grinding, the workpiece vibrates along the feed direction while the grinding wheel vibrates along its longitudinal axis. The machining system employs two ultrasonic transducers to generate vibrations that are transmitted to the grinding tool and the workpiece separately. Therefore, the tool vibration and the workpiece vibration are independent of each other. Before developing the theoretical model, the following assumptions and simplifications are made.

- The abrasive grains are evenly spaced on the grinding wheel surface and the grit shape is conical with a cone-apex angle of 60°, as shown in Fig. 2.
- The abrasive grits are rigid and their shape and size remain constant during grinding.
- The amplitude and frequency of ultrasonic vibrations superposed to the grinding wheel and workpiece keep
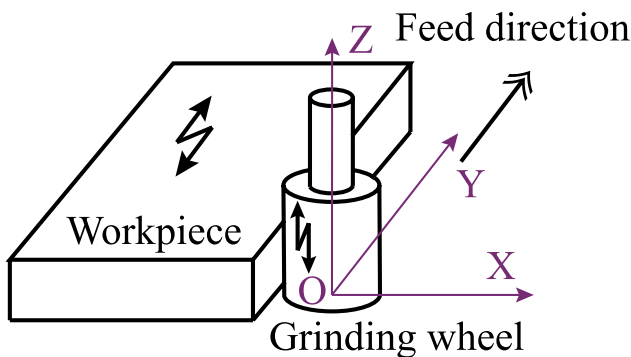

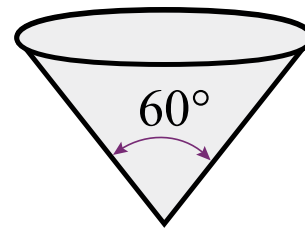**Fig. 1** Schematic diagram of two-dimensional ultrasonic-assisted grinding

Fig. 2 The shape of single abrasive grain

constant during processing, independent of load and temperature variations.

As shown in Fig. 3, the modeling process mainly contains the following four steps: (1) simplification of grinding wheel topography; (2) kinematic description; (3) determination of cutting state and trajectory point coordinate update; (4) data post-processing.

2.1.1 Simplification of grinding wheel topography

By measuring the grinding wheel morphology, Doman and Zhou et al. [21, 22] found that the protrusion height of abrasive grains follows the normal distribution. Malkin and Hwang [23] pointed out that the maximum diameter d_{max} and the average diameter d_{ave} of abrasive grits can be gained depending on the particle size M, as shown in the following equations:

$$d_{max} = 15.2M^{-1} \tag{1}$$

$$d_{ave} = 68M^{-1.4} \tag{2}$$

Based on the characteristics of the normal distribution, the mean μ, the variance σ^2, and the average distance l_{ave} between adjacent abrasive grits can be expressed as follows [11]:

$$\mu = d_{ave} \tag{3}$$

$$\sigma = (d_{max} - d_{ave})/3 \tag{4}$$

$$l_{ave} = 137.9M^{-1.4}\sqrt[3]{\pi/(32 - S)} \tag{5}$$

where $S = 32 - V_g/2$, V_g is the volume fraction of abrasive grains.

Figure 4 shows the modeling process of grinding wheel morphology. According to the above information combined with the size and shape of a grinding wheel, the distribution of abrasive grains on its surface can be obtained first. For simplification, a group of abrasive grits with the same axial position

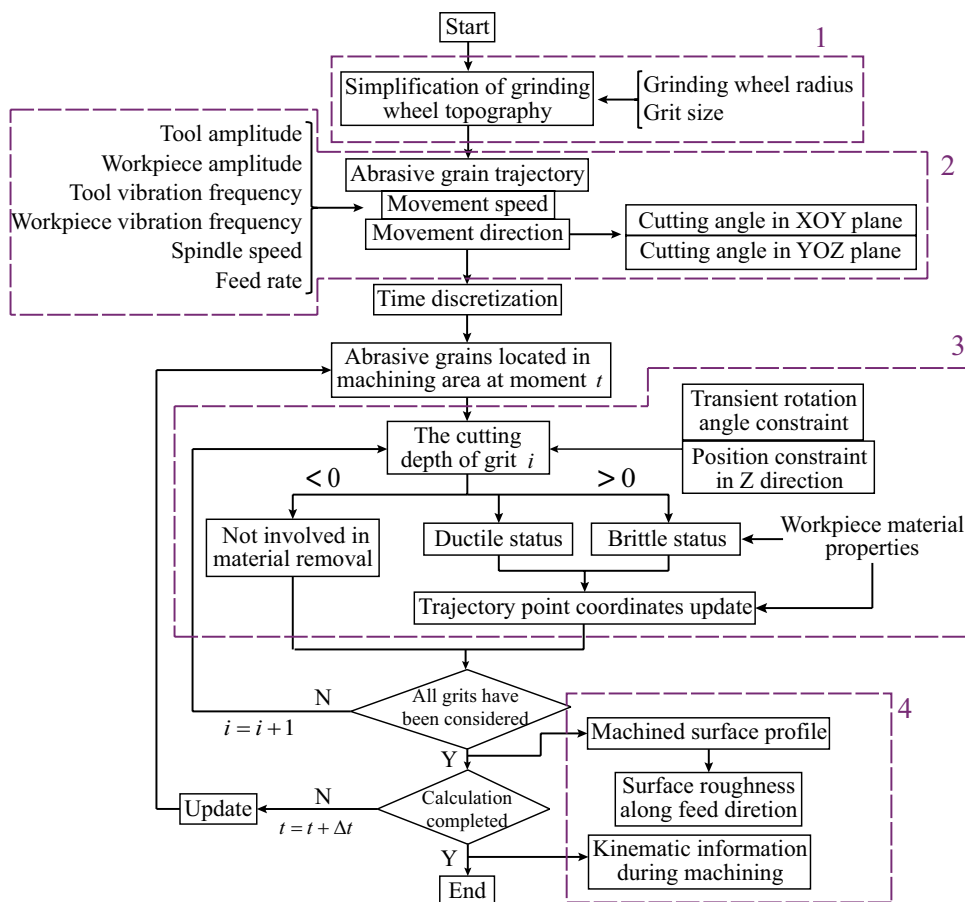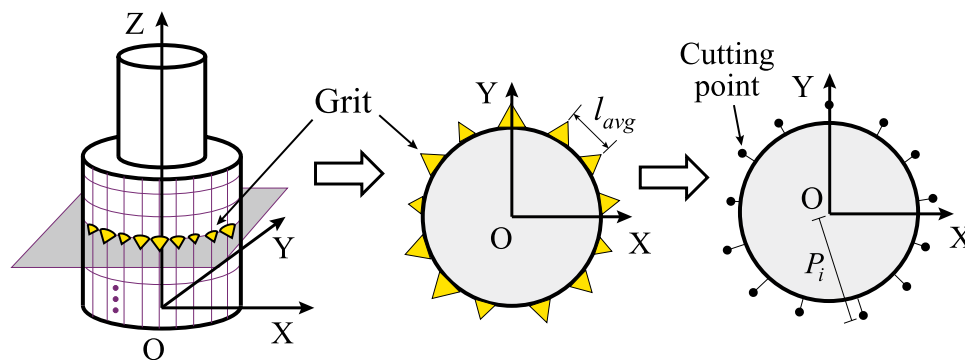**Fig. 3** Flowchart of the theoretical model

Fig. 4 Theoretical model of grinding wheel topography

on the circumference is considered and the diameter of the grits follows the normal distribution. Finally, the theoretical grinding wheel topography is gained by simplifying the abrasive grains as cutting points located at their apexes. P_i represents the rotation radius of the cutting point corresponding to grain i, which can be expressed as

$$P_i = R + \sqrt{3}d_i/2 \tag{6}$$

where R is the radius of the grinding wheel and d_i is the diameter of grain i.

2.1.2 Kinematic description

In 2D-UAG, the motion trajectory of abrasive grains becomes a complex spatial curve due to the introduction of two-dimensional ultrasonic vibration. To describe the motion track, a Cartesian coordinate system is established, as shown in Fig. 1. The origin is located at the initial position of the bottom surface center of the grinding tool and the axial direction of the grinding wheel is parallel to the Z-axis. Based on the grinding kinematics, the trajectory of individual abrasive particle can be expressed as follows;

$$\begin{cases} x_i^t = -P_i \cdot \cos(2\pi f_s t - i\psi) \\ y_i^t = P_i \cdot \sin(2\pi f_s t - i\psi) + A_W \cdot \sin(2\pi f_W t + \phi) + f \cdot t \quad (7) \\ z_i^t = z_{initial} + A_T \cdot \sin(2\pi f_T t) \end{cases}$$

where (x_i^t, y_i^t, z_i^t) is the coordinates of grain i at moment t, f_s is the spindle rotation frequency, ψ is the phase difference caused by the distance between adjacent abrasive grains, $\psi = l_{ave}/R$, A_W and f_W are the amplitude and frequency of the workpiece vibration, A_T and f_T are those of the tool vibration, ϕ is the initial phase difference between tool vibration and workpiece vibration, f is the feed rate, t is the grinding time, and $z_{initial}$ is the initial Z-coordinate of abrasive grains.

Meanwhile, the velocity of grits can be obtained as follows by deriving the above equation with respect to time:

$$\begin{cases} V_{i-x}^t = P_i \cdot 2\pi f_s \cdot \sin(2\pi f_s t - i\psi) \\ V_{i-y}^t = P_i \cdot 2\pi f_s \cdot \cos(2\pi f_s t - i\psi) + A_W \cdot 2\pi f_W \cdot \cos(2\pi f_W t + \phi) + f \\ V_{i-z}^t = A_T \cdot 2\pi f_T \cdot \cos(2\pi f_T t) \end{cases}$$
$$(8)$$

where $\overline{V_i^t} = (V_{i-x}^t, V_{i-y}^t, V_{i-z}^t)$ is the velocity of grain i at moment t.

Furthermore, to describe the motion direction of active grains relative to the workpiece, the cutting angle in XOY plane α_{i-xoy}^t and that in YOZ plane α_{i-yoz}^t are proposed in this study. As illustrated in Fig. 5, α_{i-xoy}^t represents the angle between the component vector $\overline{V_{i-xoy}^t}$ of $\overline{V_i^t}$ in the XOY plane and the direction vector $\overline{Feed}$, while the latter refers to that between the fractional vector $\overline{V_{i-yoz}^t}$ of $\overline{V_i^t}$ in the YOZ plane and $\overline{Feed}$.

2.1.3 Determination of cutting state and trajectory point coordinates update

During the grinding of hard and brittle materials, the cutting depth of individual abrasive grain determines the material removal mode at the cutting position, which further affects the cutting states of adjacent grits and the machined surface profile. Therefore, it is important to model this variable accurately for revealing the kinematic characteristics of abrasive grains and understanding the surface generation mechanism in 2D-UAG. In this study, a set of abrasive particles with the same Z-coordinate are considered in the model development and more specific information about the material removal behavior can be obtained.

Under the machining condition shown in Fig. 1, only a portion of abrasive particles on the grinding tool surface participates in the material removal. To reduce the amount of calculation, the transient rotation angle is proposed for abrasive grains.

$$\theta_i^t = (\theta_i^0 + \omega_s t) \backslash 2\pi \qquad (9)$$

where θ_i^0 is the rotation angle of grit i at $t = 0$ and ω_s is the angular speed of the spindle.

According to the positional relationship between the grinding wheel and the workpiece in the XOY plane, as shown in Fig. 5(a), the abrasive particle with a transient rotation angle in the range of $[0, \arccos((R-d)/R)]$ is in the machining area, where d represents the grinding depth of cut. In a single time step, the cutting depth of grain i located in the machining area is obtained based on the geometric relationship between its current track point and the historical track points of all abrasive grits considered in model development. The specific calculation steps are shown as follows:

- At moment t, the coordinates of the trajectory point $P_i^t(x_i^t, y_i^t, z_i^t)$ of grain i are obtained first. Then, the set of historical track points $\{P_n^{t-m \cdot t_{ter}}(x_n^{t-m \cdot t_{ter}}, y_n^{t-m \cdot t_{ter}}, z_n^{t-m \cdot t_{ter}})\}$ of all abrasive grits around P_i^t is gained according to the constraints expressed in the following equation, as schematically shown in Fig. 6.

Fig. 5 Definitions of cutting angles

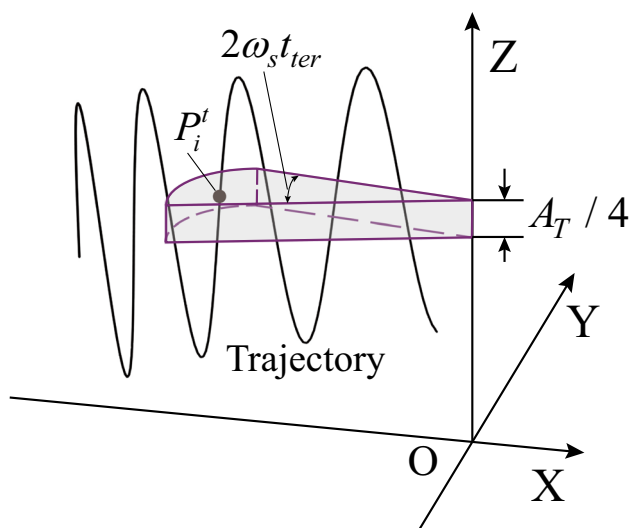**(a)** Cutting angle in XOY plane

(b) Cutting angle in YOZ plane
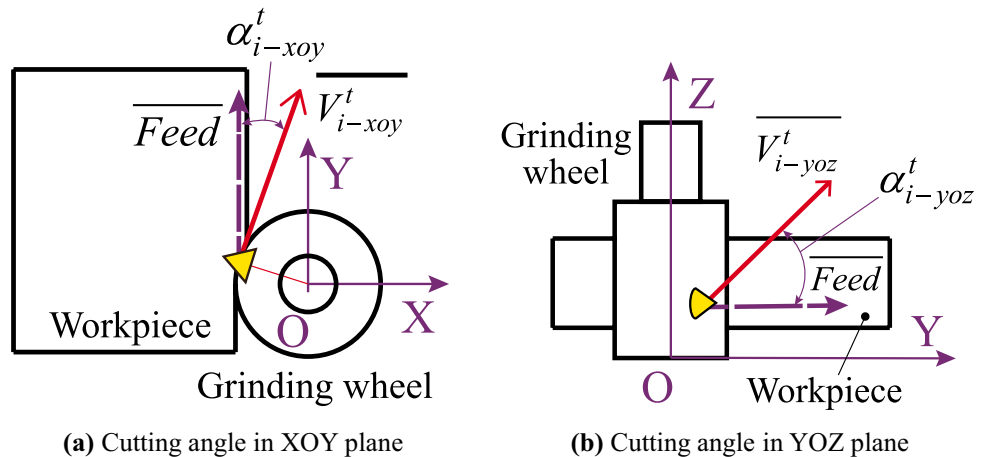
Fig. 6 Schematic diagram of constraints

$$\begin{cases} \theta_n^{t-m \cdot t_{ter}} \in [(\theta_i^t - \omega_s \cdot t_{ter}), (\theta_i^t + \omega_s \cdot t_{ter})] \\ z_n^{t-m \cdot t_{ter}} \in [(z_i^t - A_T/8), (z_i^t + A_T/8)] \end{cases} \quad (10)$$

where $m = 0, 1, 2, \cdots, t/t_{ter}$, $n = 1, 2, 3, \cdots, N$, N is the total number of abrasive grains considered in model development, and t_{ter} is the time discrete interval.

- After that, the distances between the above points and the grinding wheel axis are calculated and expressed as LP_i^t, $\{LP_n^{t-m \cdot t_{ter}}\}$.
- A new set $\{(LP_i^t - LP_n^{t-m \cdot t_{ter}})\}$ is obtained by gaining the difference between LP_i^t and each element in $\{LP_n^{t-m \cdot t_{ter}}\}$. When all elements in this new set are not greater than zero, the abrasive grain i is not involved in material removal at this moment. Otherwise, the largest element in the set is defined as the cutting depth h_i^t of grain i at moment t.

The experimental results obtained by Li et al. [6] through performing scratching tests on SiC indicated that as the cutting depth of the Berkovich indenter increased, the material removal mechanism shifted from plastic deformation to brittle fracture and the critical depth was found to be 76.034 nm. Considering that the shape of the Berkovich indenter is similar with that of actual abrasive grain, the cutting behavior in the scratching test can represent that of individual grit in a real grinding situation.

In this study, the cutting state of individual grit is classified into ductile status and brittle status according to the above information. In the former state, the material removal behavior of SiC is similar with that of metal material in the grinding process and the machined surface is formed by the trajectories of active grains. While in the brittle state, the material removal is realized by the

initiation and propagation of brittle cracks, as illustrated in Fig. 7. Under the latter machining condition, the machined surface profile does not match the trajectory of abrasive grains. To improve the modeling accuracy, the following steps are adopted to update the coordinates of trajectory points in the brittle removal mode.

- Depending on the indentation fracture mechanics, the depth of radial crack C_h is obtained as follows based on the cutting depth of abrasive grit [24].

$$C_h = (h_i^t \tan \beta)^{1+1/2b} (cH_v/K_{IC})^{1/b} (E/H_v)^{2/5b} \quad (11)$$

where β is half of the apex angle, H_v is the Vickers hardness of SiC, K_{IC} is the fracture toughness, E is the elastic modulus, $b = 0.25$, and $c = 2.88$.

- As shown in Fig. 8, the distance between the trajectory point and the grinding wheel axis is increased by C_h through moving it along the radial direction of the grinding tool. Finally, the updated coordinates can be gained as $P_i^t(x_i^t - C_h \cdot \cos \theta_i^t, y_i^t + C_h \cdot \sin \theta_i^t, z_i^t)$.

2.1.4 Data post-processing

The above calculations allow to obtain the cutting depth, cutting speed, and cutting angles of abrasive grains relative to the workpiece during material removal. The statistical
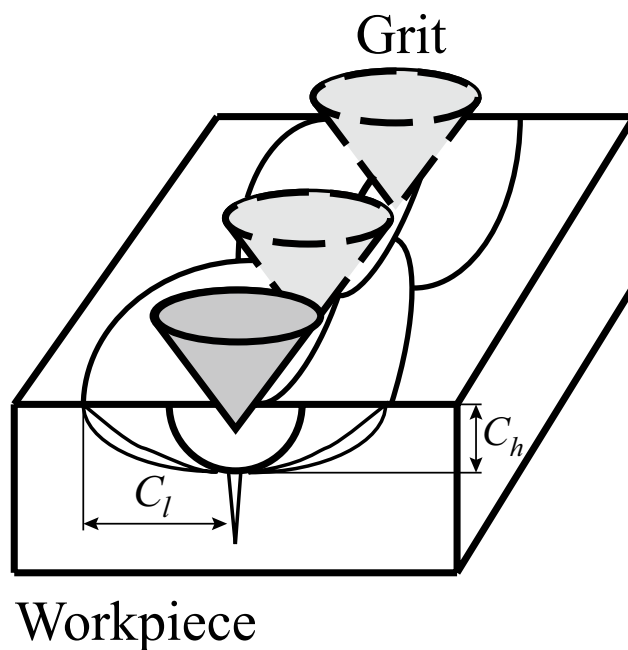

Fig. 7 Material removal process in brittle state

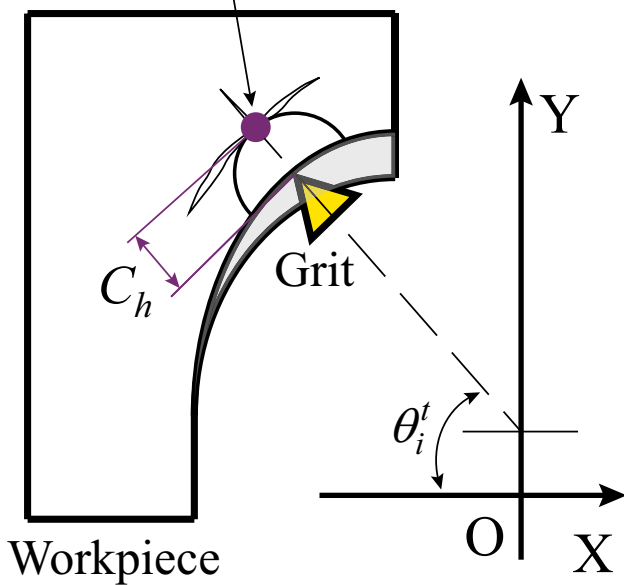Updated trajectory point in brittle removal mode

Fig. 8 Update procedure of trajectory point coordinates

features of these variables can be further gained from the raw data to reveal the kinematic characteristics of abrasive particles in 2D-UAG.

In CG, the trajectories of abrasive grits are in the XOY plane. To obtain the theoretical surface toughness, the trajectory points in the machined area with X-coordinate less than $-R$ and Y-coordinate greater than zero are classified into different sets according to their Y-coordinates. The track point with the minimum X-coordinate in each set is selected and these points connected by straight lines form the machined surface profile, as shown in Fig. 9. Z_i

represents the distance between the track point i and the baseline. According to the definitions of the arithmetic mean deviation of contour and the maximum height of a profile [16, 25], as shown in the following equations, the surface roughness of the machined surface along the feed direction can be obtained.

$$R_a = \frac{1}{n} \sum_{i=1}^{n} |Z_i| \qquad (12)$$

$$R_z = R_p + R_v \qquad (13)$$

where R_p is the maximum contour peak height and R_v represents the maximum profile valley depth.

Due to the application of tool vibration, the motion track of abrasive grits becomes a spatial curve in 2D-UAG. To gain the theoretical surface roughness value on a certain horizontal surface, the following method is used:

- For a single abrasive grit i, its historical trajectory points are first connected by straight lines in sequence. After that, the intersections of the straight-line segments and the horizontal plane are further obtained and defined as S_i^j, where j is the intersection number.
- The above procedure is performed for all considered grits and the intersection set is $\{S_i^j\}$, $i = 1, 2, \cdots, N$.
- Finally, the methodology adopted in CG is used to calculate the surface roughness based on $\{S_i^j\}$.

It is worthy to note that during the calculation, the theoretical surface roughness values in plane $z = z_{\text{initial}}$, plane $z = z_{\text{initial}} + A_T/2$, and plane $z = z_{\text{initial}} - A_T/2$ are gained and the average value is considered as the final prediction result in 2D-UAG.

Fig. 9 Theoretical machined surface profile
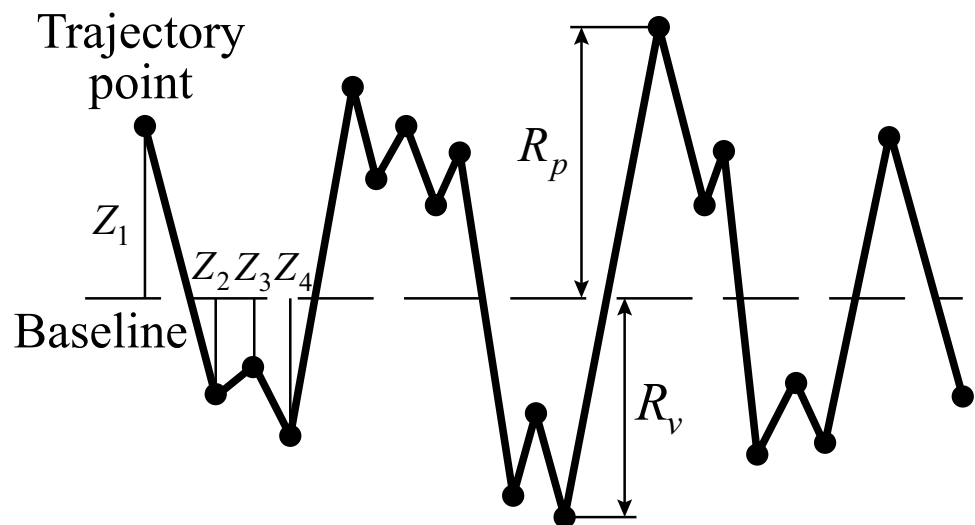
2.2 Influences of vibration parameters on the kinematic features in 2D-UAG

2.2.1 Influences of vibration amplitudes

Based on the proposed theoretical model, this section discusses the kinematic characteristic of abrasive grains under the four machining conditions shown in Table 1. The workpiece material is pressureless sintered silicon carbide with dimensions of $15 \times 15 \times 5$ mm and the detailed material properties are shown in Table 2. The electroplated diamond grinding wheel with a diameter of 8 mm and a particle size of 240# is employed. These grinding situations correspond to the four machining methods including CG, rotary ultrasonic machining (RUM) in which the ultrasonic vibration is applied to the grinding wheel along its axis, one-dimensional ultrasonic-assisted grinding (1D-UAG) in which only the workpiece vibrates along the grinding wheel feed direction, and 2D-UAG.

Figure 10 shows the calculation results. It can be seen in Fig. 10(a) that the cutting depth of abrasive grits under different machining conditions approximately follows the normal distribution. The introduction of tool vibration effectively reduces the average value of cutting depth compared with that in CG and the probability of the cutting depth in the range [0–1] increases, which are beneficial to facilitate the ductile removal of workpiece material and to improve the machined surface quality. While when the ultrasonic vibration is only superposed to the workpiece along the grinding tool feed direction, limited variation in the cutting depth distribution is found compared with that in CG. Figure 10(b) presents the cutting speed distribution of active grains. In CG, the cutting speed roughly obeys the normal distribution with a narrow distribution range, while in other three machining conditions, the cutting speed approximately follows the beta distribution. In RUM, the distribution range of cutting speed is expanded compared with CG. And due to that the ultrasonic vibration direction is perpendicular to the rotation plane of abrasive grits, the cutting speed in RUM is larger than that in CG, which is helpful to increase the dynamic fracture toughness of brittle material and to suppress the initiation and propagation of brittle cracks. In 1D-UAG, a significant expansion of the cutting speed

Table 2 Material properties

Hardness (GPa)	Density (g/cm³)	Elastic modulus (GPa)	Fracture toughness (MPa · m^{1/2})	Average particle size (μm)	Bending strength (GPa)
27.7	3.15	410	4.7	4–10	0.38

distribution range is found. However, due to that the ultrasonic vibration is introduced along the feed direction, the situation that the cutting speed of active grains is lower than the average value in CG exists with a probability of 51.69%. In 2D-UAG, the maximum and minimum cutting speeds are higher than those in 1D-UAG and the probability of the cutting speed smaller than the average velocity in CG remains almost constant. Figure 10(c) and (d) illustrate the distributions of cutting angles in different machining conditions. Under the same cutting parameters, the workpiece vibration determines the distribution characteristics of α_{i-xoy}^{t}. In 1D-UAG and 2D-UAG, the distribution range of α_{i-xoy}^{t} is larger than that in CG and RUM. While the tool vibration along with the workpiece vibration determines the distribution features of α_{i-yoz}^{t}. In this study, the α_{i-yoz}^{t} in 2D-UAG has the largest distribution range among the four machining methods. The expanded distribution range of α_{i-xoy}^{t} facilitates the propagation of brittle cracks in multiple directions and enhances the interference among cracks, which are beneficial to prevent cracks from expanding into the workpiece and to reduce the depth of the subsurface damage layer. The increase in the distribution range of α_{i-yoz}^{t} strengthens the interference among grain trajectories and this phenomenon generally reduces the cutting depth of grits and grinding forces.

Figure 11 shows the kinematic characteristics of a typical grit under different processing conditions. As shown in Fig. 11(a), the cutting depth of the grit increases monotonically with spindle rotation in CG, while this variable in 1D-UAG fluctuates periodically and the fluctuation amplitude gradually goes up. In RUM and 2D-UAG, cyclical variations in the cutting depth can be found and the maximum value in a single fluctuation cycle is close to the average value in CG in the same time interval and the minimum

Table 1 Machining conditions with different ultrasonic amplitudes

No	Method	Cutting parameters	Tool amplitude (μm)	Workpiece amplitude (μm)	Ultrasonic frequency (kHz)	Phase difference (°)
1	CG	Spindle speed: 4000 r/min	0	0	–	–
2	RUM	Feed rate: 60 mm/min	5	0	30	–
3	1D-UAG	Grinding depth of cut: 45 μm	0	5	30	–
4	2D-UAG		5	5	30	0

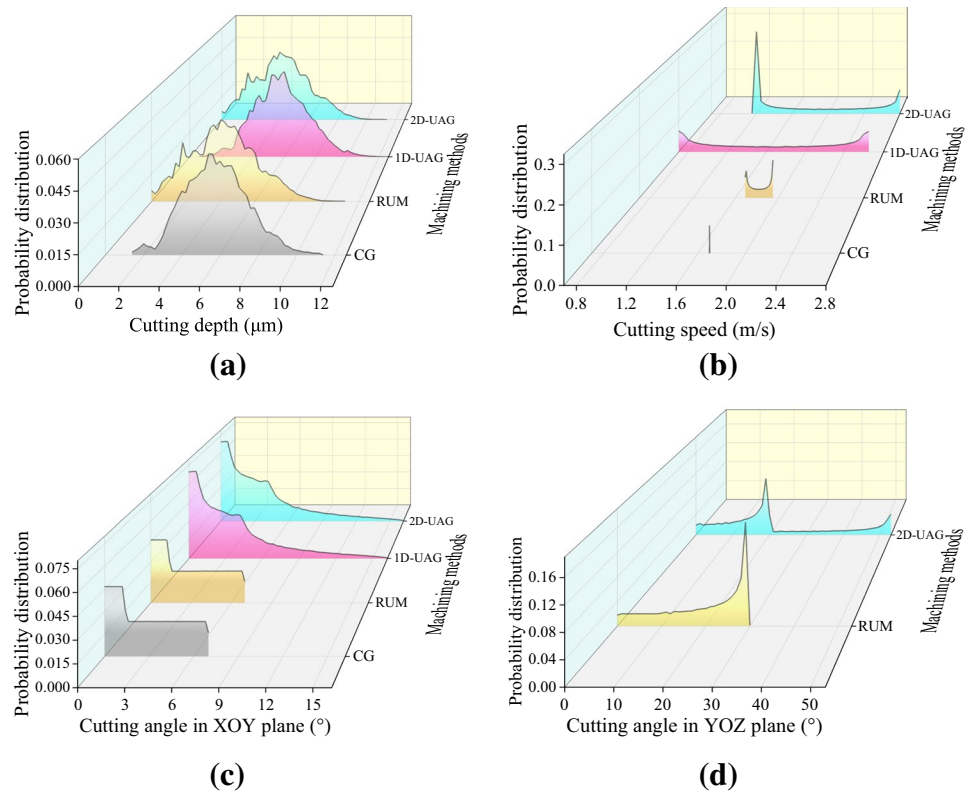**Fig. 10** Influences of machining methods on kinematic features of abrasive grains
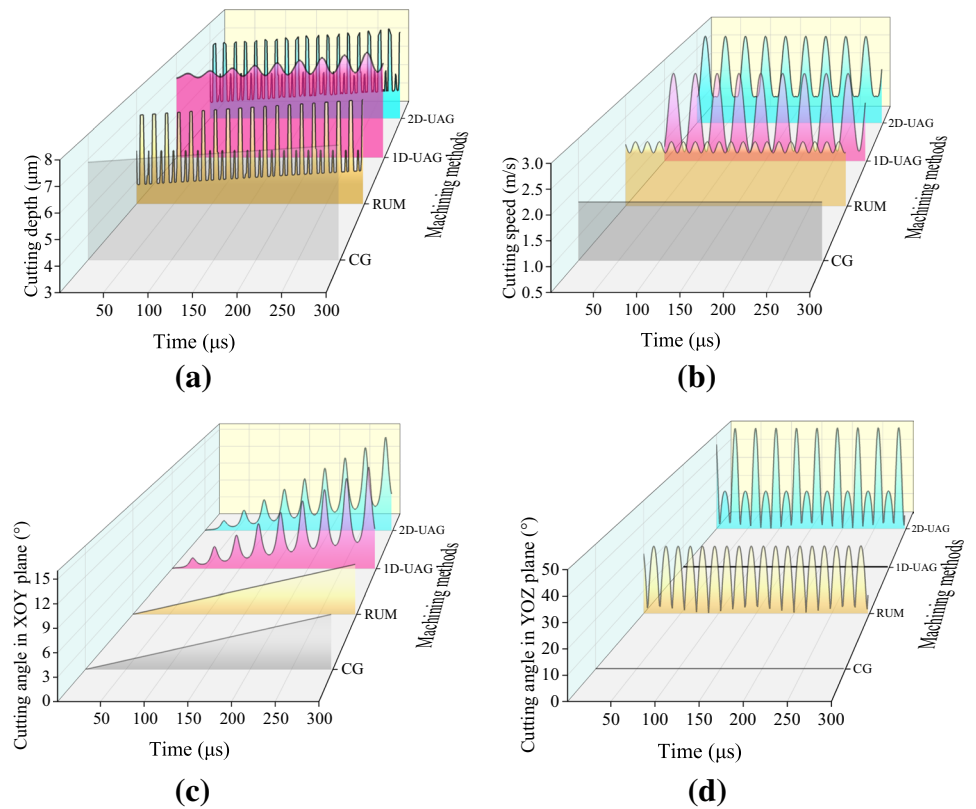

Fig. 11 Influences of machining methods on kinematic features of individual grit

value is approximately 54% of that. Furthermore, the average cutting depth in a single cycle increases slowly with the grinding time. Figure 11(b) presents the cutting speed of the grit under each processing condition. In CG, the abrasive grain completes material removal with a constant cutting speed, while, in other machining methods, the cutting speed fluctuates periodically with different amplitudes. In RUM, the cutting speed is slightly higher than that in CG. The variation trends of the cutting speed in 1D-UAG and 2D-UAG are similar with larger fluctuation ranges compared with that in RUM. In one fluctuation cycle, part of the cutting speed in 1D-UAG and 2D-UAG is lower than that in CG and the maximum and minimum cutting speeds in 2D-UAG are greater than those in 1D-UAG. Figure 11(c) shows the variation trend of α_{i-xoy}^{t} during material removal process. As discussed above, the workpiece vibration determines the trend of the cutting angle in the XOY plane. Thus, in CG and RUM, α_{i-xoy}^{t} varies in the same manner, increasing monotonically with the grinding time. While, in 1D-UAG and 2D-UAG, α_{i-xoy}^{t} presents a periodical fluctuation with increasing variation magnitude. Meanwhile, the average α_{i-xoy}^{t} in one fluctuation cycle increases with the increase of grinding time. Figure 11(d) shows the variation trends of α_{i-yoz}^{t} in the four machining methods. As shown in the figure, in CG and 1D-UAG, α_{i-yoz}^{t} remains constant at zero due to that no tool vibration is introduced. While, in RUM and 2D-UAG, α_{i-yoz}^{t} fluctuates cyclically with grinding time and the maximum value of α_{i-yoz}^{t} in 2D-UAG is 1.69 times greater than that in RUM, which results from the introduction of two-dimensional ultrasonic vibration.

2.2.2 Influences of phase difference in 2D-UAG

When the tool and the workpiece vibrate at the same frequency in 2D-UAG, the phase difference between the vibrations has important influences on the trajectory and cutting behavior of abrasive grains. This subsection reveals the effects of phase difference on the kinematic characteristics in the machining process from a statistical point of view. The discussed working conditions are shown in Table 3.

As shown in Fig. 12(a), the cutting depth of abrasive grains still roughly follows the normal distribution under

different working conditions and the phase difference has little effect on that. Figure 12(b) presents the distribution of cutting speed, indicating that the distribution characteristics are similar when the phase difference is 45° or 90° or 135°. For a phase difference of 0°, the minimum cutting speed is increased by about 48% and the probability of the cutting speed in [1.15, 1.5] is increased by 2.4 times compared with that in the other three conditions. Meanwhile, the probability of the cutting speed located in [2.5, 2.8] remains basically the same. Figure 12(c) demonstrates that the influences of phase difference on the distribution of α_{i-xoy}^{t} are limited and can be ignored. The effects of phase difference on the distribution of α_{i-yoz}^{t} are shown in Fig. 12(d). The distribution characteristics of this variable are highly similar for the phase difference of 45° and 135°. When the phase difference is 0°, the maximum value of α_{i-yoz}^{t} increases by 10% and the value corresponding to the probability peak decreases by 17% compared to that with a phase difference of 45°. For the machining condition where the phase difference is 90°, the distribution range of α_{i-yoz}^{t} is the smallest and the probability of the range [25–35] is about 47%.

2.2.3 Influences of vibration frequencies in 2D-UAG

Vibration frequency is an important ultrasonic parameter in 2D-UAG, which has a significant effect on the motion trajectory of abrasive grains during the grinding process. This subsection focuses on revealing the influences of vibration frequencies on the kinematic features of multiple grits in 2D-UAG and the four working conditions discussed are shown in Table 4.

As shown in Fig. 13(a), the vibration frequencies of the tool and workpiece have limited effect on the distribution of cutting depth which still roughly follows the normal distribution with highly similar distribution curves under different working conditions. Figure 13(b) shows the effect of vibration frequencies on the cutting speed distribution of abrasive grits. The distribution characteristics of this variable are similar in groups 1 and 4 where the tool and the workpiece vibrate at the same frequency. On the other hand, in the latter case, the distribution range of the cutting speed is wider. Compared to group 1, the minimum cutting speed

Table 3 Machining conditions with different phase differences

No	Cutting parameters	Ultrasonic frequency (kHz)	Ultrasonic amplitude (μm)	Phase difference (°)
1	Spindle speed: 4000 r/min	30	5	0
2				45
3	Feed rate: 60 mm/min			90
4	Grinding depth of cut: 45 μm			135

Fig. 12 Influences of phase difference on kinematic features of abrasive grains
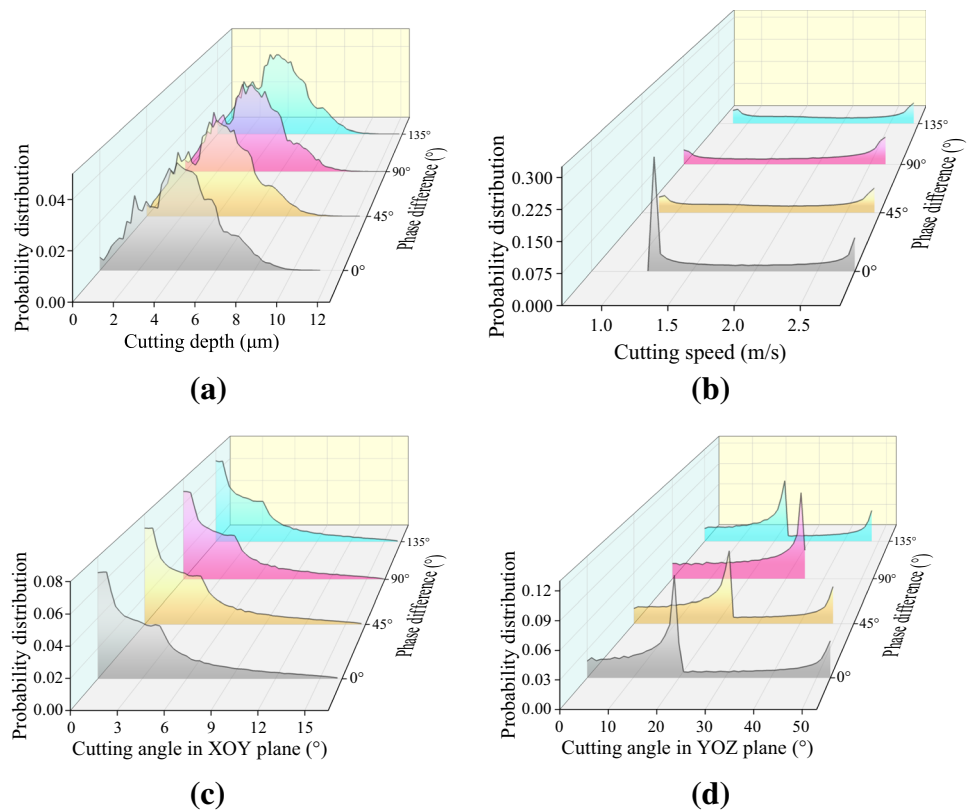

(a)

(b)

(c)

(d)

**Table 4** Machining conditions with different vibration frequencies

No	Cutting parameters	Vibration frequency of grinding wheel (kHz)	Vibration frequency of workpiece (kHz)	Ultrasonic amplitude (μm)	Phase difference (°)
1	Spindle speed: 4000 r/min	15	15	5	0
2		15	30		–
3	Feed rate: 60 mm/min Grinding depth of cut: 45 μm	30	15		–
4		30	30		0

in group 4 is reduced by 10.85% and the maximum one is increased by 26.13%. In addition, the cutting speed in group 1 is mainly distributed in the interval $[1.29, 1.6] \cup [2, 2.22]$, while that in group 4 is mainly located in the range of $[1.15, 1.4] \cup [2.4, 2.8]$. The distribution curves of cutting speed in groups 2 and 3 have a similar form and a wider distribution range is found in the former machining condition. Compared with that in group 3, the minimum value of cutting speed in group 2 declines by 41.67% and the maximum value increases by 13.92%.

Figure 13(c) illustrates the effect of ultrasonic frequencies on the distribution of α^t_{i-xoy}. It can be seen that α^t_{i-xoy} has almost the same distribution curve in groups 1 and 3 due to the identical workpiece vibration parameters. The same phenomenon is found in groups 2 and 4. The comparison of the distribution features of α^t_{i-xoy} in groups 1 and 2 indicates that increasing the workpiece vibration frequency can effectively increase the maximum value of α^t_{i-xoy} and thus extend the distribution range of this variable. As shown in Fig. 13(d), the vibration frequencies have significant effects on the distribution of α^t_{i-yoz}. The comparison of the distribution curves in groups 1 and 4 demonstrates that the distribution features of α^t_{i-yoz} are similar when the tool and the workpiece vibrate at the same frequency and increasing the vibration frequency can effectively expand the distribution range of this variable. Furthermore, the α^t_{i-yoz} in group 2 and that in group 3 have the same distribution range. However, in the former machining condition, the α^t_{i-yoz} is mainly distributed in the range of

Fig. 13 Influences of ultrasonic frequencies on kinematic features of abrasive grains

(a)

(b)

(c)

(d)
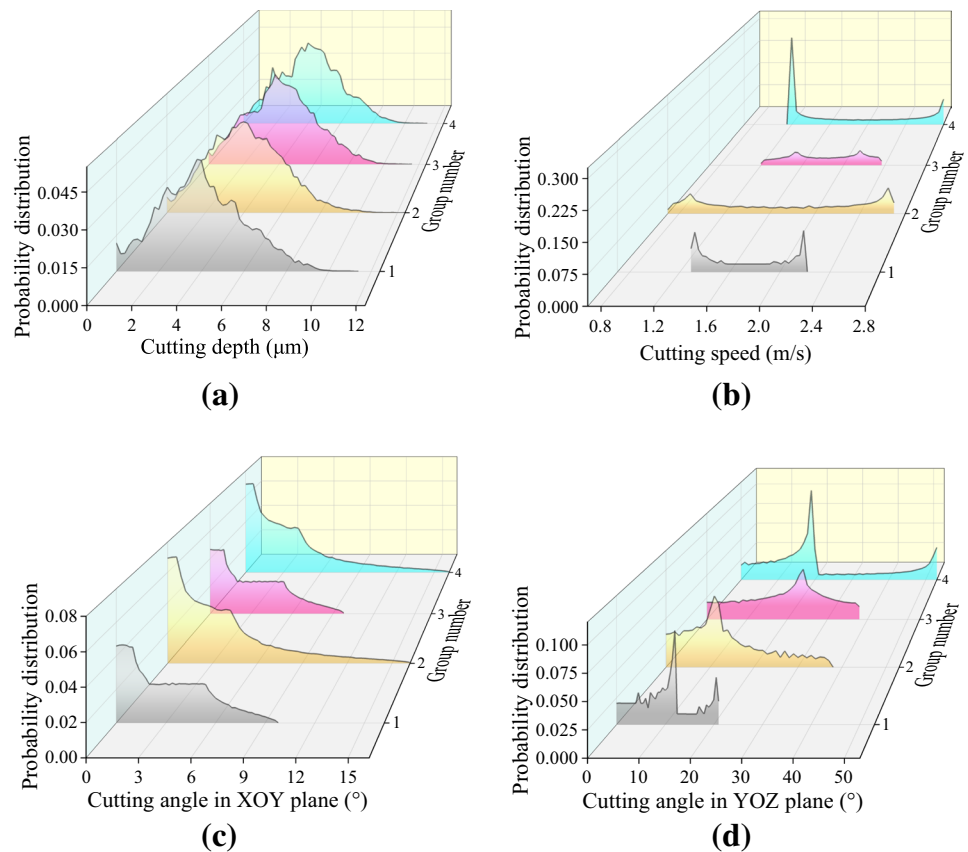
[0–20], while this variable in the latter is mainly located in the interval [15, 38].

3 Experimental details

To verify the theoretical model proposed in this study indirectly by obtaining the prediction accuracy of surface roughness, a series of grinding experiments are conducted on a G-VM5 machine tool and the experimental apparatuses are illustrated in Fig. 14. During the experiment, a weak sinusoidal signal is first generated by the signal generator (DG1022U, RIGOL, China) and then its amplitude is amplified to a target level through the power amplifier (1040 L, E&I, USA) to drive the ultrasonic transducer. The matching units (Lo-Hi-Z-8–500, E&I, USA) are used to realize the impedance matching between the power amplifier and the load and to achieve tuning matching. The 2D-UAG machining system consists of a self-designed RUM device and an ultrasonic transducer. The former transmits ultrasonic vibration to the grinding tool during machining. With the support of an L-shape part, the ultrasonic transducer is horizontally placed with its longitudinal axis parallel to the grinding wheel feed direction. A stage is held by the output end of the transducer and the workpiece is glued on this stage by epoxy

resin. Through the above setup, the ultrasonic vibration can be superposed to the workpiece along the feed direction. A laser vibrometer (LV-S01-ST, Sunny Instruments, Singapore) is employed to measure the vibration amplitudes of the grinding wheel and workpiece before experiments and the output amplitudes of the machining device can be adjusted by changing the driving voltage.

The workpiece material properties and the grinding wheel parameters are consistent with those in theoretical analyses. Three groups of grinding experiments are performed to reveal the influences of ultrasonic vibration parameters on the surface roughness and the microscopic morphology of machined surfaces. The detailed machining parameters are presented in Tables 1, 3, and 4.

After grinding, the stage and workpiece are first placed in an ultrasonic cleaning machine with acetone solution to dissolve the glue and remove the chips. After that, a profilometer (IF G5, Alicona, Austria) is used to obtain the surface roughness. Three regions on the machined surface are randomly selected for measurement and the surface roughness values along the feed direction and its vertical direction are obtained respectively. The average value of the three measurements is taken as the result. In addition, a scanning electron microscope (JSM-IT300, JEOL, Japan) is employed to observe the micro topography of machined surfaces.

Fig. 14 Experimental apparatuses
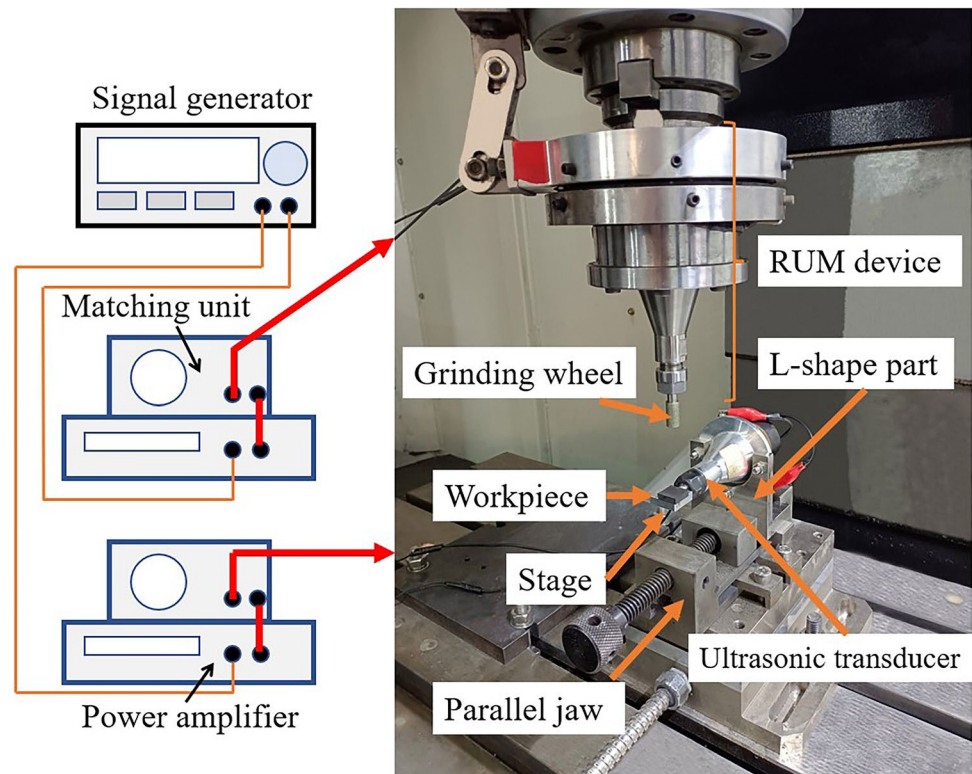

4 Results and discussion

4.1 Model verification and surface roughness

Figures 15 and 16 illustrate the effects of ultrasonic parameters on surface roughness where subscript 1 refers to the measurements along the Y-axis and subscript 2 indicates those along the Z-axis. In Figs. 15(c) and 16(c), the group numbers correspond to the four machining conditions shown in Table 3. It can be seen that the variation trends of Ra and Rz are similar with changing machining parameters and under the same processing condition, the surface roughness value in Z-direction is larger than that in Y-direction. Figure 15 indicates that the predicted values of Ra_1 and Rz_1 are consistent with the experimental ones and the prediction error is limited within 10.06% with an average value of 6.03%. The following reasons may be responsible for the above deviations. First, the influences of the random distribution features of abrasive grains and the coupling effects among adjacent grits along the Z-axis are ignored in the model development. Secondly, the variations in workpiece material properties resulted from the change of grinding speed and the impact behaviors of abrasive particles are not considered. Attributed to the introduction of ultrasonic vibrations in 2D-UAG, the average value of cutting depth decreases effectively and the distribution ranges of α_{i-xoy}^t and α_{i-yoz}^t expand significantly.

Therefore, 2D-UAG can obtain the lowest surface roughness among the four processing methods under the same cutting parameters. Specifically, Ra_1 and Ra_2 obtained in 2D-UAG reduce by 28.66% and 38.21% respectively compared with those in CG. In addition, under the machining conditions discussed in this section, the surface roughness in RUM is slightly lower than that in 1D-UAG, as shown in Figs. 15(a) and 16(a).

When the tool and the workpiece vibrate at the same frequency, the phase difference between the vibrations has non-negligible influences on the surface roughness. As illustrated in Figs. 15(b) and 16(b), as the phase difference increases from 0 to 90°, Ra_1 presents a continuous increasing trend with a maximum growth of 17.09%, while when the phase difference further increases to 135°, Ra_1 reduces by 7.67%. The similar variation trend of Ra_2 with increasing phase difference is found. By comparing the data shown in Fig. 12 with the above variation trends of surface roughness, it can be inferred that the distribution range of α_{i-yoz}^t has important influences on the surface quality in 2D-UAG and expanding that is beneficial to reduce the surface roughness. Figures 15(c) and 16(c) show the influences of ultrasonic frequencies on the surface roughness. In grinding conditions where the vibration frequencies of the grinding tool and workpiece are the same, increasing the ultrasonic frequency from 15 to 30 kHz can reduce Ra_1 by 11.03% and decrease Ra_2 by 22.5%. Furthermore, when

Fig. 15 Effects of ultrasonic parameters on the surface roughness along Y-direction

(a) Influences of ultrasonic amplitudes

(b) Influences of phase difference
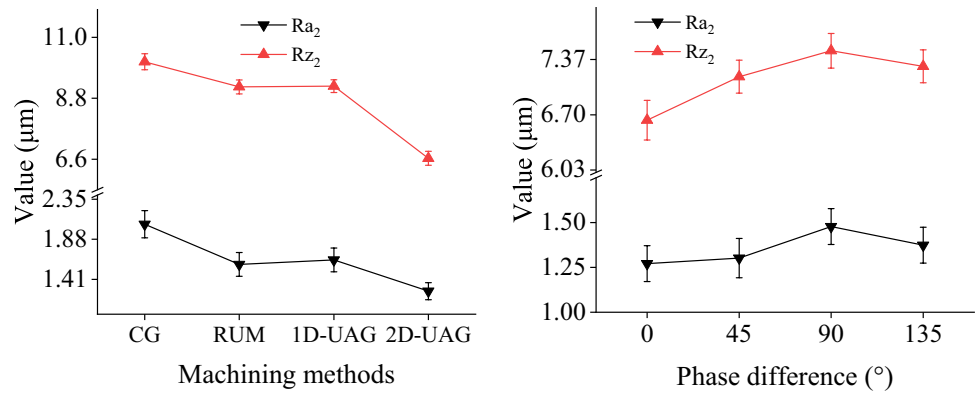
(c) Influences of ultrasonic frequencies
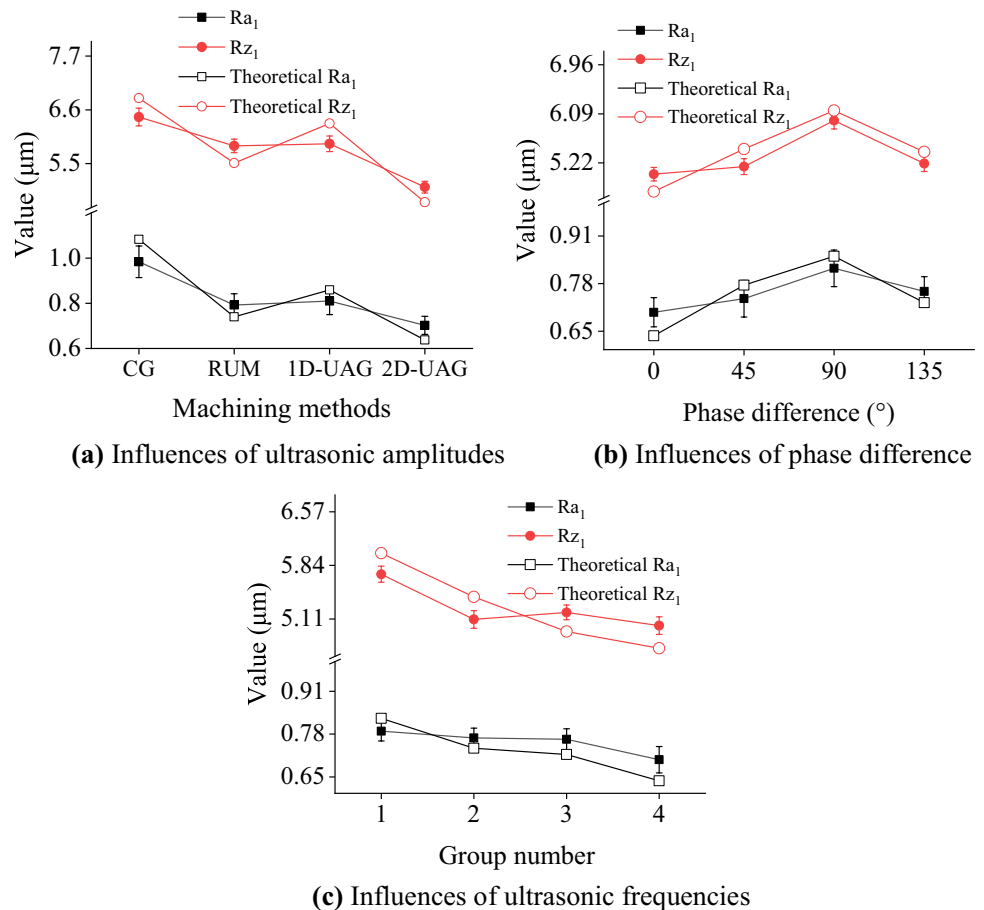
the vibration frequency of the workpiece is twice that of the grinding tool, the exchange of vibration frequencies between them has a limited influence on Ra_1, while Ra_2 reduced by 5.08% with that. The above experimental results and the kinematic features of abrasive grains shown in Fig. 13 indicate that for groups 1 and 4, the expanded distribution ranges of cutting speed, α_{i-xoy}^t and α_{i-yoz}^t are conducive to decrease the surface roughness, while for groups 2 and 3, although the cutting speed and α_{i-xoy}^t in group 2 have wider distribution scopes, the influences of these factors on Ra_1 can be ignored. The reasons leading to the reduction of Ra_2 will be discussed in the following parts.

4.2 Micro morphology

Figure 17 shows the microscopic morphology of the machined surface obtained by 2D-UAG. It demonstrates that the ductile and brittle removal behaviors of SiC coexist during the grinding process and the brittle removal mode dominates in the machining conditions discussed in this study. Two distinct regions can be found on the machined surface including the ductile removal dominant region and the brittle removal dominant region, as shown in Fig. 17(b) and (c, d). In the latter region, the material removal is realized by the nucleation and propagation of brittle cracks. A large number of small-scale fracture traces with uneven morphology and micro-cracks can be observed on the machined surface. Large-scale fractures also occur in some locations and the fracture surface is flat and smooth with parallel stripes, as shown in Fig. 17(d). Meanwhile, discrete black regions exist on the ground surface, which are the graphite phases in workpiece material [9]. By observing the subsurface morphology, Dai and Li et al. [9, 26] revealed the damage formation mechanism of SiC during grinding, as shown in Fig. 18. Under the extrusion of abrasive grains, dislocations are first generated in SiC grains and move toward the grain boundary. On the other hand, grain boundaries and phase boundaries in the material generally lead to dislocation pile-ups. When the stress caused by this phenomenon exceeds the critical tensile stress, brittle cracks initiate on the boundaries and propagate through the grain, forming micro-pits on the machined surface. Furthermore, when the cutting depth of abrasive grains is relatively large, the greater external load will facilitate partial cracks across the grain boundaries and expand to the SiC grains away from the machined

Fig. 16 Effects of ultrasonic parameters on the surface roughness in Z-direction

(a) Influences of ultrasonic amplitudes

(b) Influences of phase difference
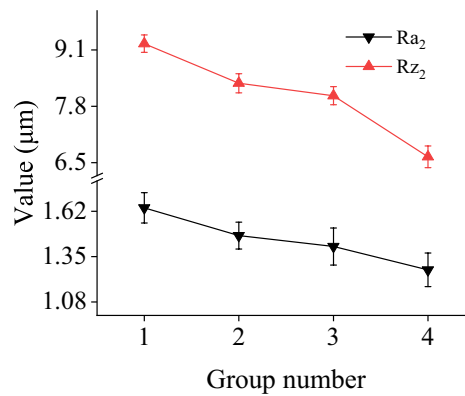
(c) Influences of ultrasonic frequencies

surface, which leads to material spalling and generates large pits on the ground surface, while the stripes on the fracture surface may be formed by slip bands. In the ductile removal dominant region, part of the material is removed by plastic deformation, similar to that of metal material during grinding. In 2D-UAG, the trajectory of abrasive grains becomes a spatial curve attributed to the introduction of ultrasonic vibrations. Thus, intersecting curved ploughing stripes can be formed on the machined surface, as shown in Fig. 17(b). In addition, the number of micro-cracks is significantly reduced in this region.

The microscopic topographies of machined surfaces obtained by different processing methods under the same cutting parameters are shown in Fig. 19. In CG and 1D-UAG, the α_{i-yoz}^t of abrasive grits is constantly zero, which means that the projection lines of the grit trajectories on the YOZ plane are parallel to each other. Since the abrasive grains are distributed on the grinding wheel surface with different protrusion heights, parallel grooves with large depths are formed on the machined surface by the grits with higher protrusion heights, as shown in Fig. 19(a) and (c). The presence of these grooves is the main reason causing that the surface roughness in

Z-direction is larger than that in Y-direction. In addition, micro-pits tend to exist at the wave crest, while the machined surface at the wave trough tends to be relatively flat and smooth. In RUM, the grinding wheel vibrates along its axis and the distribution range of α_{i-yoz}^t is effectively expanded. This phenomenon is beneficial to suppress the adverse effects of the inconsistent protrusion height of abrasive grits. As shown in Fig. 19(b), although deep grooves still exist on the machined surface, the surface roughness values in Z-direction presented in Fig. 16(a) indicate that the groove depth generated in RUM is reduced compared with that in CG. Meanwhile, the micro-pit size at the wave crest on the machined surface is also reduced due to the decrease in the average cutting depth of abrasive grains in RUM, as shown in Fig. 10(a). This phenomenon further leads to the reduction of the surface roughness in Y-direction. In 2D-UAG, attributed to the introduction of two-dimensional ultrasonic vibration, the trajectory of abrasive grits becomes more complicated and the distribution range of α_{i-yoz}^t is further enlarged, which enhance the coupling effects among abrasive grains and are beneficial to improve the machined surface quality. As shown in Fig. 19(d), the

Fig. 17 Microscopic morphologies of machined surface obtained by 2D-UAG

(a) Surface morphology

(b) Ductile removal dominant region

(c) Brittle removal dominant region

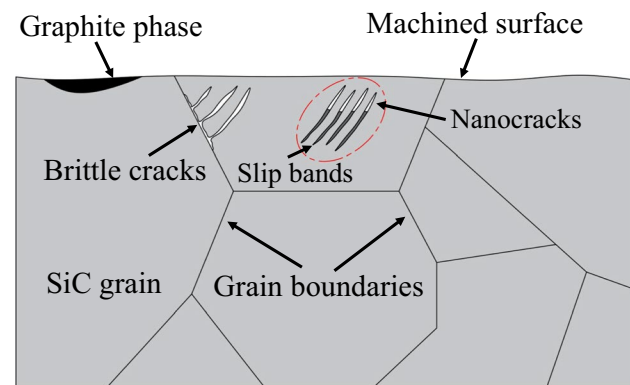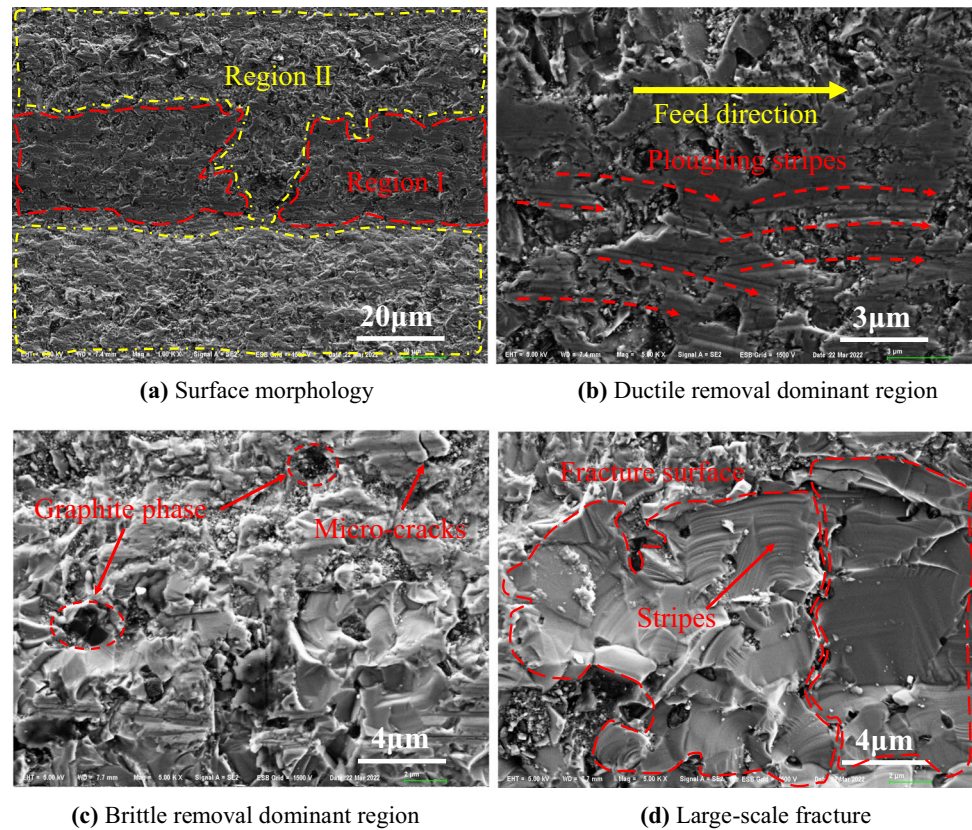**(d)** Large-scale fracture

Fig. 18 Schematic diagram of the damage formation mechanism

number of grooves on the machined surface obtained by 2D-UAG is effectively reduced and the depth of grooves also decreases. In addition, the comparison between Figs. 17 and 19 indicates that the alteration of the grinding method did not significantly change the material removal mode and the surface damage form.

Figure 20 shows the influences of phase difference on the microscopic morphology of machined surfaces when the tool and workpiece vibrate at the same frequency. As the phase difference increases from 0 to 90°, the number and depth of grooves on the machined surface gradually increase.

Combined with the data shown in Figs. 15(b) and 16(b), it can be inferred that the above phenomenon leads to the increase of the surface roughness. For the phase difference of 45° and 135°, the surface morphologies are similar to each other. As shown in Fig. 12, the influences of the phase difference on the distribution features of cutting depth, cutting speed, and α_{i-xoy}^{t} are relatively limited. On the other hand, the distribution range of α_{i-yoz}^{t} decreases first and then increases with the increasing phase difference and the minimum value is achieved when the phase difference is 90°. The above results demonstrate that the expansion in the distribution scope of α_{i-yoz}^{t} is conducive to reduce the surface roughness and improve the surface quality in 2D-UAG.

Figure 21 presents the effects of ultrasonic frequencies on the surface morphologies in 2D-UAG. When both the grinding wheel and the workpiece vibrate at 15 kHz in group 1, deep grooves reappear on the machined surface and material spalling can be found in localized regions. As illustrated in Fig. 21(d), simultaneously increasing the vibration frequencies of the grinding tool and the workpiece to 30 kHz can effectively improve the surface quality through decreasing the groove depth and suppressing material spalling. As discussed above, the machining quality improvement is mainly attributed to the expansion in the distribution range of α_{i-yoz}^{t}. Meanwhile, as the vibration frequencies increase, the

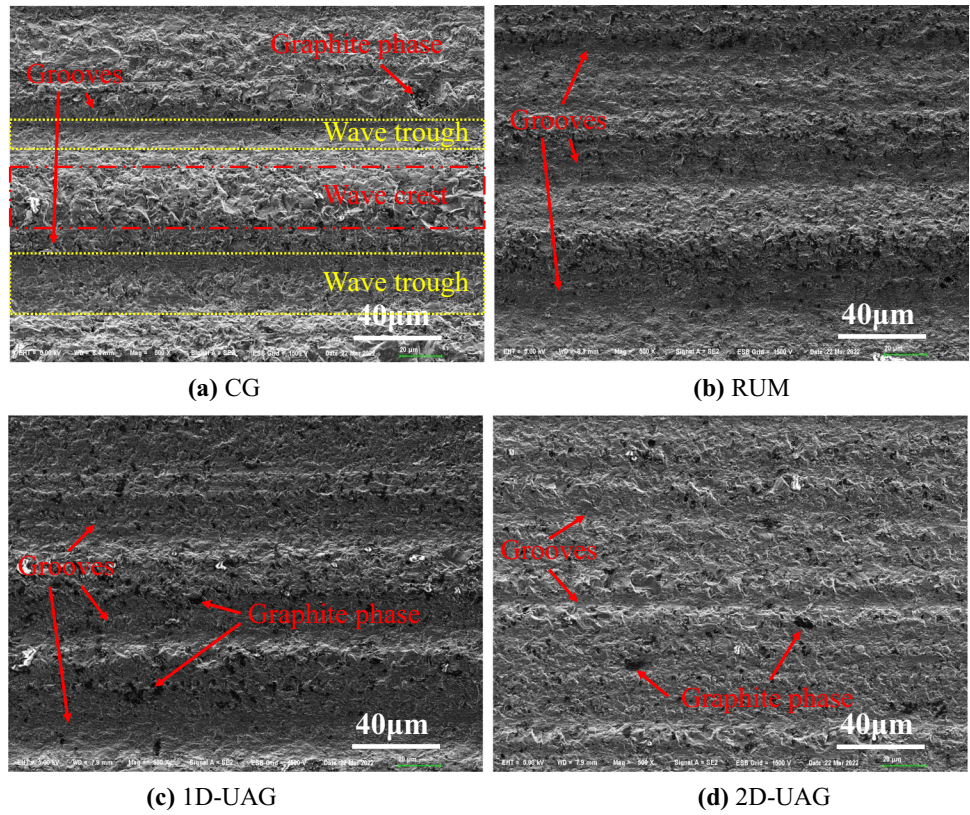**Fig. 19** Microscopic topographies obtained by different machining methods

(a) CG

(b) RUM

(c) 1D-UAG

(d) 2D-UAG

Fig. 20 Effects of phase difference on the microscopic morphologies in 2D-UAG

(a) 0°

(b) 45°

(c) 90°

(d) 135°
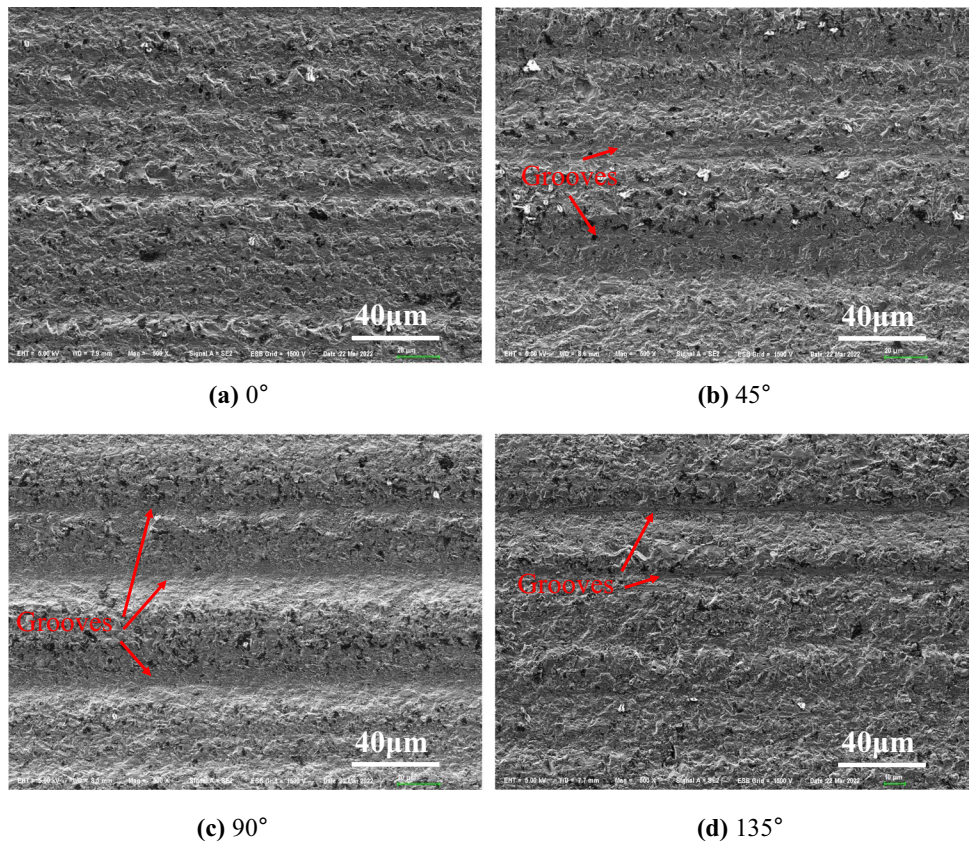
Fig. 21 Influences of ultrasonic frequencies on the microscopic topographies in 2D-UAG

(a) Group 1

(b) Group 2

(c) Group 3

(d) Group 4
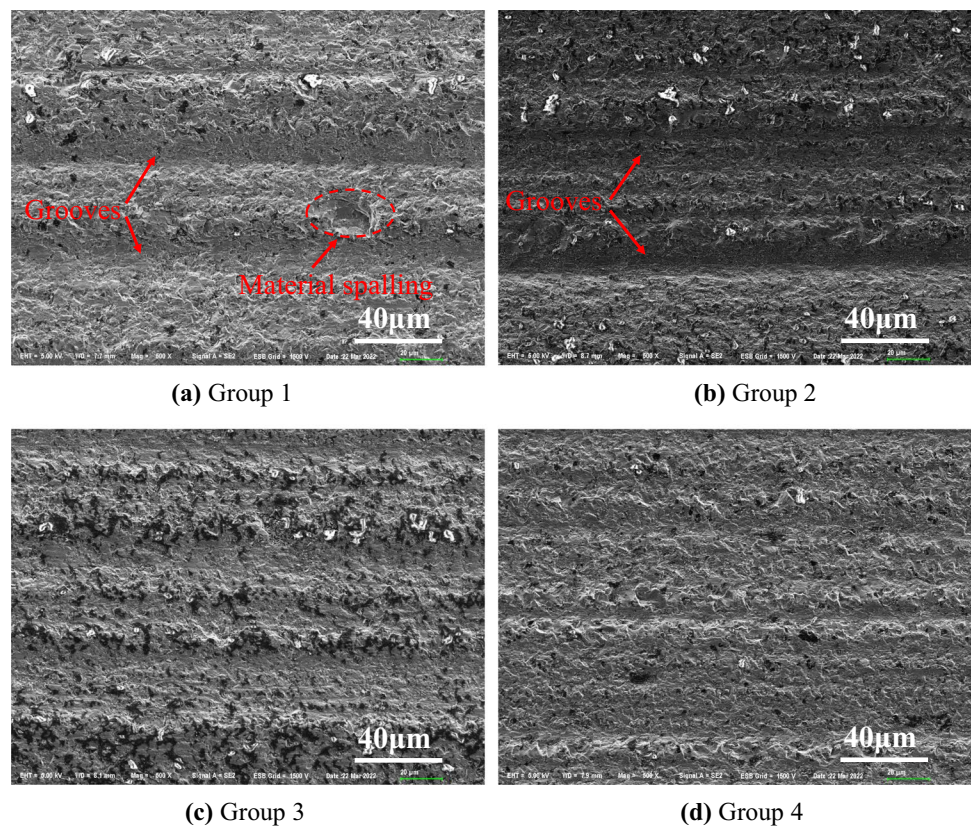
maximum values of cutting speed and α^t_{i-xoy} are also increased by 26.13% and 65.31%, which are beneficial to inhibit crack growth and further suppress the machining damage. Figure 21(b) and (c) combined with the data shown in Fig. 16(c) demonstrate that comparing with doubling the workpiece vibration frequency, doubling the tool vibration frequency is more helpful to improve the surface uniformity, which results from the reduction in groove depth on the machined surface. As mentioned above, the data shown in Fig. 13 indicates that the cutting speed and α^t_{i-xoy} in group 2 have wider distribution ranges than those in group 3, while the α^t_{i-yoz} in group 3 has the same distribution range as that in group 2 with a larger average value. Considering that the effects of the former factor on Ra_1 are limited under the machining conditions of groups 2 and 3, it can be inferred that the increase in the average value of α^t_{i-yoz} also helps to improve the machined surface quality and reduce the surface roughness in Z-direction.

5 Conclusions

To reveal the surface generation mechanism in 2D-UAG of SiC, a numerical model considering the coupling behavior of abrasive grains and the material removal mechanism is proposed in this study. To describe the motion direction of active grains relative to the workpiece, the cutting angles in the XOY plane and YOZ plane are defined in the model development. This theoretical model is capable to obtain the effects of ultrasonic vibration parameters on the kinematic characteristics of multiple grits from a statistical point of view and to predict the surface roughness. After that, validation experiments are conducted and the microscopic morphologies of machined surfaces obtained under different machining conditions are gained. The major conclusions are as follows;

1. The proposed model is validated experimentally and the prediction error of surface roughness along the feed direction is limited within 10.06%.
2. In the four machining methods including CG, RUM, 1D-UAG, and 2D-UAG, the cutting depth of abrasive grains approximately follows the normal distribution. The average value of cutting depth in 2D-UAG decreases by 23.5% compared with that in CG. Under the same cutting parameters, the workpiece vibration determines the distribution characteristics of α^t_{i-xoy}, while the tool vibration and workpiece vibration jointly determine the distribution features of α^t_{i-yoz}. Meanwhile, the introduction of ultrasonic vibrations significantly alters the dis-

tribution range and characteristics of cutting speed. When the tool and workpiece vibrate at the same frequency in 2D-UAG, the phase difference has a significant effect on the distribution of α_{i-yoz}^{t}. As the phase difference increases from 0 to 90°, the distribution range of α_{i-yoz}^{t} declines by 34.62%. In addition, increasing the ultrasonic frequency from 15 to 30 kHz can enlarge the distribution range of cutting speed and α_{i-yoz}^{t} by 88.89% and 152.38%, respectively.

3. With the change of machining conditions, the variation trends of Ra_1, Rz_1, Ra_2, and Rz_2 are similar. For the same cutting parameters, Ra_1 obtained by 2D-UAG reduces by 28.66% compared to that in CG. When the vibration frequencies of the grinding tool and workpiece are the same, the influence of phase difference cannot be ignored. Ra_1 shows a continuous upward trend with a maximum increment of 17.09% as the phase difference grows from 0 to 90°. However, Ra_1 decreases by 7.67% as the phase difference further increases to 135°. Furthermore, with the ultrasonic vibration frequency increasing from 15 to 30 kHz, Ra_1 reduces by 11.03%.

4. In the machining conditions where the electroplated diamond grinding wheel with a particle size of 240# is used, the SiC is removed mainly by brittle fracture with surface damages including micro-pits with different sizes, micro-cracks, and material spalling. Under the same cutting parameters, by adjusting the ultrasonic vibration parameters rationally, the machining quality in 2D-UAG can be improved through reducing the number and depth of grooves and the brittle fracture size on the machined surface. Among the kinematic parameters mentioned above, the distribution range of α_{i-yoz}^{t} has the greatest influence on the ground surface quality and surface roughness.

Author contribution Hongbo Li: methodology, investigation, and writing—original draft preparation. Tao Chen: writing— review and editing, and supervision. Zhenyan Duan: writing—original draft preparation, validation, and visualization. Yiwen Zhang: data curation. Haotian Li: software and formal analysis.

Data availability The data and material in this study are available from the corresponding author upon reasonable request.

Code availability The source code in this study is available from the corresponding author upon reasonable request.

Declarations

Ethics approval Not applicable.

Consent to participate Not applicable.

Consent for publication All authors have agreed to publish this manuscript.

Conflict of interest The authors declare no competing interests.

References

1. Dai C, Yin Z, Wang P, Miao Q, Chen J (2021) Analysis on ground surface in ultrasonic face grinding of silicon carbide (SiC) ceramic with minor vibration amplitude. Ceram Int 47(15):21959–21968. https://doi.org/10.1016/j.ceramint.2021.04.214

2. Meng B, Yuan D, Xu S (2019) Coupling effect on the removal mechanism and surface/subsurface characteristics of SiC during grinding process at the nanoscale. Ceram Int 45(2):2483–2491. https://doi.org/10.1016/j.ceramint.2018.10.175

3. Yang Z, Zhu L, Zhang G, Ni C, Lin B (2020) Review of ultrasonic vibration-assisted machining in advanced materials. Int J Mach Tools Manuf 156:103594. https://doi.org/10.1016/j.ijmachtools.2020.103594

4. Ning F, Cong W (2020) Ultrasonic vibration-assisted (UV-A) manufacturing processes: State of the art and future perspectives. J Manuf Process 51:174–190. https://doi.org/10.1016/j.jmapro.2020.01.028

5. Cao S, Li HN, Huang W, Zhou Q, Lei T, Wu C (2022) A delamination prediction model in ultrasonic vibration assisted drilling of CFRP composites. J Mater Process Technol 302:117480. https://doi.org/10.1016/j.jmatprotec.2021.117480

6. Li C, Zhang F, Meng B, Liu L, Rao X (2017) Material removal mechanism and grinding force modelling of ultrasonic vibration assisted grinding for SiC ceramics. Ceram Int 43(3):2981–2993. https://doi.org/10.1016/j.ceramint.2016.11.066

7. Cao J, Wu Y, Lu D, Fujimoto M, Nomura M (2014) Material removal behavior in ultrasonic-assisted scratching of SiC ceramics with a single diamond tool. Int J Mach Tools Manuf 79:49–61. https://doi.org/10.1016/j.ijmachtools.2014.02.002

8. Liu Y, Li B, Wu C, Kong L, Zheng Y (2018) Smoothed particle hydrodynamics simulation and experimental analysis of SiC ceramic grinding mechanism. Ceram Int 44(11):12194–12203. https://doi.org/10.1016/j.ceramint.2018.03.278

9. Dai J, Su H, Wang Z, Xu J, Fu Y, Chen J (2021) Damage formation mechanisms of sintered silicon carbide during single-diamond grinding. Ceram Int 47(20):28419–28428. https://doi.org/10.1016/j.ceramint.2021.06.259

10. Chen JB, Fang QH, Wang CC, Du JK, Liu F (2016) Theoretical study on brittle–ductile transition behavior in elliptical ultrasonic assisted grinding of hard brittle materials. Precis Eng 46:104–117. https://doi.org/10.1016/j.precisioneng.2016.04.005

11. Yang Z, Zhu L, Ni C, Ning J (2019) Investigation of surface topography formation mechanism based on abrasive-workpiece contact rate model in tangential ultrasonic vibration-assisted CBN grinding of ZrO2 ceramics. Int J Mech Sci 155:66–82. https://doi.org/10.1016/j.ijmecsci.2019.02.031

12. Cao Y, Yin J, Ding W, Xu J (2021) Alumina abrasive wheel wear in ultrasonic vibration-assisted creep-feed grinding of Inconel 718 nickel-based superalloy. J Mater Process Technol 297:117241. https://doi.org/10.1016/j.jmatprotec.2021.117241

13. Zhou W, Tang J, Shao W (2020) Modelling of surface texture and parameters matching considering the interaction of multiple rotation cycles in ultrasonic assisted grinding. Int J Mech Sci 166:105246. https://doi.org/10.1016/j.ijmecsci.2019.105246

14. Setti D, Arrabiyeh PA, Kirsch B, Heintz M, Aurich JC (2020) Analytical and experimental investigations on the mechanisms of surface generation in micro grinding. Int J Mach Tools Manuf 149:103489. https://doi.org/10.1016/j.ijmachtools.2019.103489

15. Zhang X, Yang L, Wang Y, Lin B, Dong Y, Shi C (2020) Mechanism study on ultrasonic vibration assisted face grinding of hard and brittle materials. J Manuf Process 50:520–527. https://doi.org/10.1016/j.jmapro.2020.01.003

16. Wu J, Cheng J, Gao C, Yu T, Guo Z (2020) Research on predicting model of surface roughness in small-scale grinding of brittle materials considering grinding tool topography. Int J Mech Sci 166:105263. https://doi.org/10.1016/j.ijmecsci.2019.105263

17. Sun Y, Su Z, Jin L, Gong Y, Ba D, Yin G, Liu M (2021) Modelling and analysis of micro-grinding surface generation of hard brittle material machined by micro abrasive tools with helical chip pocket. J Mater Process Technol 297:117242. https://doi.org/10.1016/j.jmatprotec.2021.117242

18. Zhou W, Tang J, Shao W (2020) Study on surface generation mechanism and roughness distribution in gear profile grinding. Int J Mech Sci 187:105921. https://doi.org/10.1016/j.ijmecsci.2020.105921

19. Zhou W, Tang J, Chen H, Shao W (2019) A comprehensive investigation of surface generation and material removal characteristics in ultrasonic vibration assisted grinding. Int J Mech Sci 156:14–30. https://doi.org/10.1016/j.ijmecsci.2019.03.026

20. Wang Q, Liang Z, Wang X, Bai S, Yeo SH, Jia S (2020) Modelling and analysis of generation mechanism of micro-surface topography during elliptical ultrasonic assisted grinding. J Mater Process Technol 279:116585. https://doi.org/10.1016/j.jmatprotec.2019.116585

21. Doman DA, Warkentin A, Bauer R (2006) A survey of recent grinding wheel topography models. Int J Mach Tools Manuf 46(3–4):343–352. https://doi.org/10.1016/j.ijmachtools.2005.05.013

22. Zhou X, Xi F (2002) Modeling and predicting surface roughness of the grinding process. Int J Mach Tools Manuf 42(8):969–977. https://doi.org/10.1016/S0890-6955(02)00011-1

23. Malkin S, Hwang TW (1996) Grinding mechanisms for ceramics. CIRP Ann 45(2):569–580. https://doi.org/10.1016/S0007-8506(07)60511-3

24. Lankford J (1982) Indentation microfracture in the Palmqvist crack regime: implications for fracture toughness evaluation by the indentation method. J Mater Sci Lett 1:493–495

25. He CL, Zong WJ, Cao ZM, Sun T (2015) Theoretical and empirical coupled modeling on the surface roughness in diamond turning. Mater Des 82:216–222. https://doi.org/10.1016/j.matdes.2015.05.058

26. Li Z, Zhang F, Zhang Y, Luo X (2017) Experimental investigation on the surface and subsurface damages characteristics and formation mechanisms in ultra-precision grinding of SiC. Int J Adv Manuf Technol 92(5):2677–2688. https://doi.org/10.1007/s00170-017-0267-4